iScience

CellPress
OPEN ACCESS

Article

Telomeres cooperate in zygotic genome activation by affecting *DUX4/Dux* transcription

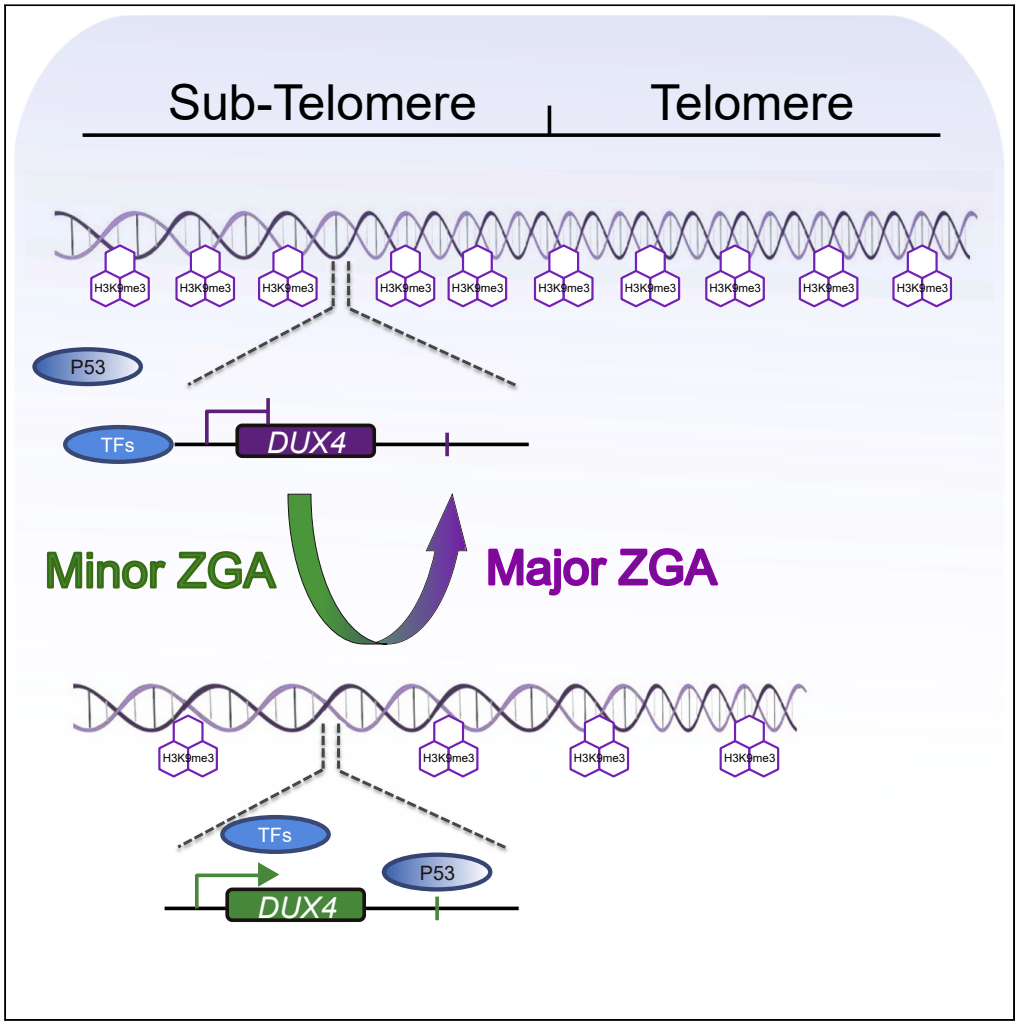

Xiaorui Zhang, Changquan Zhang, Di Zhou, ..., Ge Lin, Sicong Zeng, Lizhi Leng

linggf@hotmail.com (G.L.)
zengsicong@hunnu.edu.cn (S.Z.)
lenglizhi.csu@163.com (L.L.)

Highlights

Telomere length undergoes remodeling during the process of ZGA

The expression of *DUX4/Dux* was negatively correlated with telomere length

H3K9me3 acted as a TPE effector in *DUX4* expression by influencing the binding of p53

Zhang et al., iScience *26*, 106158
March 17, 2023
https://doi.org/10.1016/j.isci.2023.106158

iScience

CellPress
OPEN ACCESS

Article

Telomeres cooperate in zygotic genome activation by affecting *DUX4/Dux* transcription

Xiaorui Zhang,[1,2,4,5,6] Changquan Zhang,[3,6] Di Zhou,[3,4] Tianlei Zhang,[2] Xueqin Chen,[3] Jinlin Ren,[1] Caixia He,[3,4] Fei Meng,[2] Qinwei Zhou,[2] Qiaohui Yang,[3] Congling Dai,[2,3] Ge Lin,[2,3,4,*] Sicong Zeng,[1,2,4,7,*] and Lizhi Leng[2,3,4,*]

SUMMARY

Zygotic genome activation (ZGA) is initiated once the genome chromatin state is organized in the newly formed zygote. Telomeres are specialized chromatin structures at the ends of chromosomes and are reset during early embryogenesis, while the details and significance of telomere changes in preimplantation embryos remain unclear. We demonstrated that the telomere length was shortened in the minor ZGA stage and significantly elongated in the major ZGA stage of human and mouse embryos. Expression of the ZGA pioneer factor *DUX4/Dux* was negatively correlated with the telomere length. ATAC sequencing data revealed that the chromatin accessibility peaks on the *DUX4* promoter region (i.e., the subtelomere of chromosome 4q) were transiently augmented in human minor ZGA. Reduction of telomeric heterochromatin H3K9me3 in the telomeric region also synergistically activated *DUX4* expression with p53 in human embryonic stem cells. We propose herein that telomeres regulate the expression of *DUX4/Dux* through chromatin remodeling and are thereby involved in ZGA.

INTRODUCTION

Zygotic genome activation (ZGA), which is an initial critical event in the life of an organism, denotes the transition from maternal-to-zygotic genomic control and the onset of transcription after fertilization so as to establish totipotentiality.[1] After several rapid cleavages during the initial stage of embryonic development, maternally stored RNAs and proteins are cleared, and the zygotic genome is then activated. The initial low level of transcription is called minor ZGA, and is then followed by a burst of transcription called major ZGA[2,3] (Figure 1A). Although the underlying mechanisms of activation require further elucidation, an analysis of the molecular spectrum of activities in mouse and human preimplantation embryos has been developed.

In early embryos, the expression of *DUX4/Dux* is activated as a key inducer in the initial stage of ZGA, and it, in turn, activates hundreds of genes in the cleavage-stage embryo, including *KDM4E*, *ZSCAN4,* and the *PRAMEF* family of genes, as well as endogenous retroviral components such as MERVL in mouse and HERVL in humans.[2,4,5] Likewise, overexpression of *Dux* in mouse embryonic stem cells resulted in an increase in the number of cells converted to an embryo-like state referred to as two-cell-like cells (2CLCs). Human *DUX4* is localized to the subtelomeric region 4q35.2 with a D4Z4 repeat of approximately 10–100 units that encodes a homeodomain transcription factor. In contrast to its role in early embryonic development, expression of *DUX4* in adult muscle tissue is responsible for facioscapulohumeral muscular dystrophy (FSHD) that is characterized by progressive and selective weakness and atrophy of facial, scapular, and humeral muscles.[6] Moreover, *DUX4* expression is inversely proportional to the telomere length in myoblasts/myotubes derived from patients with FSHD.[7] It is speculated that the release of the telomere position effect (TPE) caused by age-related telomere erosion may be one of the key factors contributing to *DUX4* expression in muscle cells of patients with FSHD.

Telomeric chromatin is generally considered to be heterochromatic. Heterochromatin is nucleated at specific genomic sites and spreads across extended chromosomal domains to promote gene silencing,[8] and the transcriptional repression induced by the spread of telomeric heterochromatin is known as TPE.[9–11] Telomeres and subtelomeric regions harbor specific post-translational histone modifications[12] that

[1]Hospital of Hunan Guangxiu, Hunan Normal University, Hunan 410001, China

[2]Reproductive and Genetic Hospital of Citic-Xiangya, Hunan 410008, China

[3]NHC Key Laboratory of Human Stem and Reproductive Engineering, School of Basic Medical Science, Central South University, Changsha, China

[4]Hunan International Scientific and Technological Cooperation Base of Development and Carcinogenesis, Changsha, China

[5]Department of Reproductive Medicine, The First Affiliated Hospital of Xi'an Jiaotong University, Xi'an, Shaanxi 710061, China

[6]These authors contributed equally

[7]Lead contact

*Correspondence: linggf@hotmail.com (G.L.), zengsicong@hunnu.edu.cn (S.Z.), lenglizhi.csu@163.com (L.L.)

https://doi.org/10.1016/j.isci.2023.106158

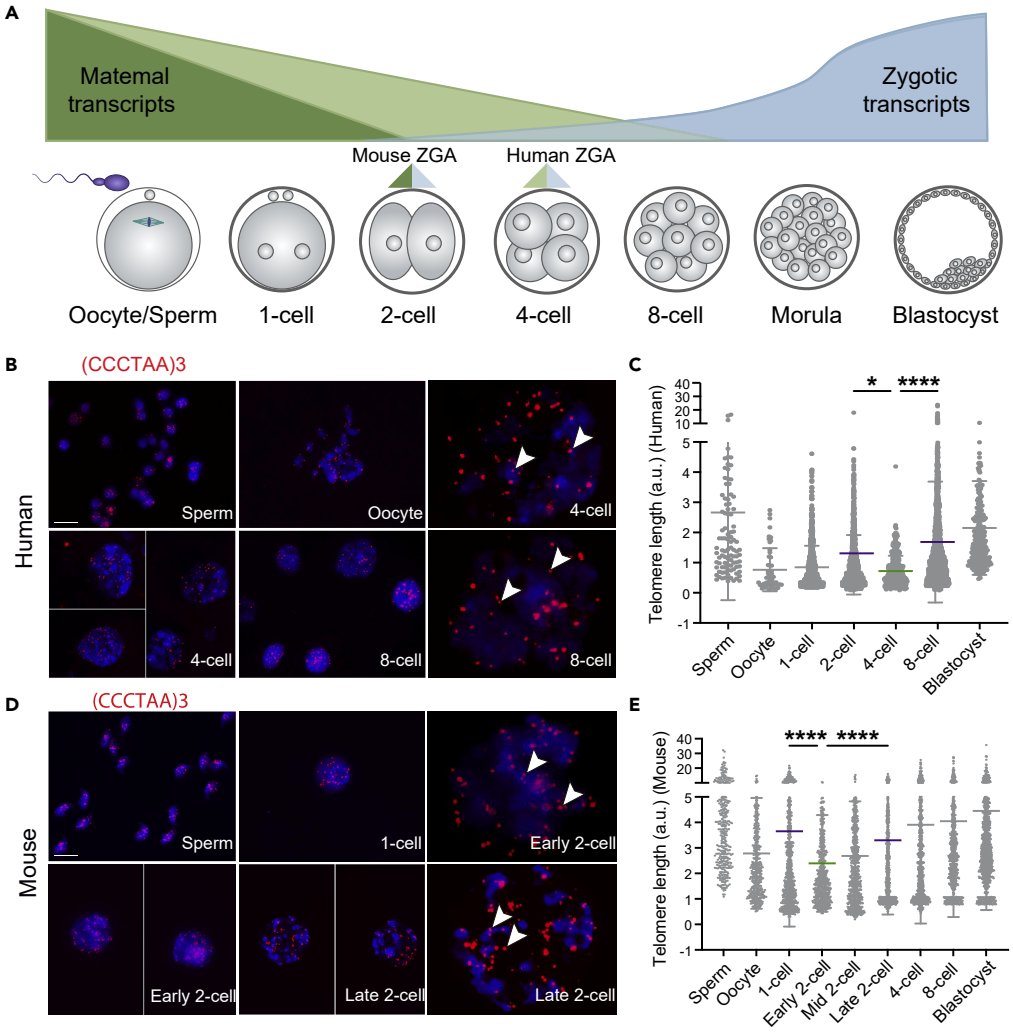

Figure 1. Spatiotemporal characterization of the telomere length and *DUX4*/*Dux* gene expression in early embryos

(A) The process referred to as the maternal-zygotic transition (MZT) encompasses the degradation of maternal material and the activation of the embryo's own genome. MZT is conserved across all species, with ZGA occurring at the two-cell stage in mice and the four-cell stage in humans.

(B) Q-FISH analysis of the telomere length in human gametes and preimplantation embryos. The red spots (white arrows) designate telomeres, and nuclei are counterstained with DAPI (blue).

(C) Telomere length is provided in arbitrary units of fluorescence (a.u.), and each stage contains five embryos. Bars represent mean ± SD. Two-tailed unpaired test. *$p < 0.05$, ****$p < 0.0001$.

(D) Q-FISH analysis of the telomere length in mouse gametes and preimplantation embryos. The red spots (white arrows) represent telomeres, and nuclei are counterstained with DAPI (blue).

(E) Telomere length is provided in arbitrary units of fluorescence (a.u.), and each stage contains five embryos. Bars represent mean ± SD. Two-tailed unpaired test. ****$p < 0.0001$.

impede accessibility from surrounding regions, and they are considered to be the primary mechanism subserving TPE regulation of gene expression. H3K9me3 and H4K20me3 are characteristic heterochromatic marks on telomeres and subtelomeres,[13,14] and their abundances change dynamically with telomere length during early embryonic development and the early expansion of pluripotent cells.[15] The extent of the influence of telomeric heterochromatin is proportional to its length; the longer the telomere, the more pronounced the TPE.[16,17] In mammals, maintenance of telomere length can be achieved by telomerase, which catalyzes the addition of TTAGGG repeats to the chromosomal terminus, and/or by chromosomal recombination-based extension of telomeric DNA sequences, termed alternative lengthening of telomeres

(ALT).[18] For germ cells, although spermatogonia manifest telomerase activity, the oocyte lacks it, resulting in long telomeres in sperm but short telomeres in eggs.[19] Thus, the telomere length adaptation may be required during early zygotic genome formation and embryonic development. In fact, some investigators have observed that telomeric repeat fragments increase greatly during preimplantation development.[20] Resetting of the telomere length has been observed in mouse implantation embryos and considered to be related to genuine pluripotency.[21–23] However, the details with respect to variations in telomere length and the role of telomere-length remodeling in early embryos remain unclear.

Herein, we examined the telomere lengths of human and mouse preimplantation embryos and found telomere length to be shortened in the minor ZGA stage and significantly elongated in the major ZGA stage. Expression of the ZGA pioneer factor *DUX4*/*Dux* was also negatively correlated with telomere length. We speculated that telomere remodeling may thus be involved in the ZGA process by participating in the regulation of *DUX4/Dux* gene expression.

RESULTS

Remodeling of telomere length in human and mouse ZGA

Early animal embryos undergo extensive reprogramming and chromatin remodeling to allow the conversion of terminally differentiated gametes to totipotent cells,[24] and telomeres have been observed to be lengthened at the two- to four-cell stage in early mouse embryos.[22,23] To characterize the dynamics of telomeres during preimplantation development, we assessed telomere length in gametes and early embryos by telomere-specific quantitative fluorescence *in situ* hybridization (Q-FISH). Sperm telomeres in human embryos were significantly longer than those in oocytes (Figures 1B and 1C). Moreover, telomeres were shortened at the two- to four-cell stage, significantly lengthened at the four- to eight-cell stage, and then gradually extended further to the blastocyst stage (Figures 1B and 1C). It is notable that human embryos initiated minor ZGA at the two- to four-cell stage, with low levels of transcription, whereas they undergo major ZGA at the four- to eight-cell stage, which involves widespread transcription of embryonic genes (Figure 1A). To further explore the relationship between telomeres and ZGA, we tracked the variations in telomere length in mouse preimplantation embryos. Similar to the case for human sperm and oocytes, the telomeres of mouse sperm were markedly longer than those of oocytes (Figures 1D and 1E). As one-cell to early-two-cell mouse embryos experience minor ZGA and mid-to-late two-cell embryos undergo major ZGA, we divided the developmental stages of two-cell embryos into early, middle, and late stages that corresponded to G1/S, S, and G2/M DNA replication phases, respectively; this then accurately reflected the process of ZGA.[25] We chose SIN3A staining expression as a marker of mouse two-cell embryonic progression, following previous studies showing the potential of SIN3A as a marker of different stages of embryonic development[26] (Figure S1A). Our Q-FISH results showed that the telomere length of mouse embryos was shortened at the one- to early-two-cell stage and extended at the early- to later-two-cell stage (Figures 1D and 1E). Collectively, our data suggest that early human and mouse embryos undergo telomere length remodeling with shortening at the minor ZGA and lengthening at the major ZGA.

The expression of *DUX4/Dux* is negatively correlated with telomere length

The expression of *DUX4*, a pioneer factor of ZGA, was reported to be associated with telomere length in FSHD[7] and was activated in our telomere-shortened placental mesenchymal stem cells derived from a patient with dyskeratosis congenita[27] (Figure S1B); we speculated that telomeres were involved in *DUX4* regulation in ZGA. To investigate the relationship between telomere remodeling and *DUX4* expression we examined the expression of *DUX4* in human embryos, and our data showed that the expression of *DUX4* was elevated at the two- to four-cell stage and sharply abrogated at the eight-cell stage (Figure S1C), consistent with a previous single-cell RNA sequencing (scRNA-seq) dataset from human early embryos[28,29] (Figure S1D). Similarly, qPCR results revealed that *Dux* (the *DUX4* paralog gene) was expressed in mouse embryos at the early two-cell stage and then rapidly declined, indicating a highly transient expression pattern (Figure S1E); this was congruent with the scRNA-seq dataset from early mouse embryos[30] (Figure S1F). These data indicated that the expression of pioneer factor *DUX4*/*Dux* was negatively correlated with telomere length.

Major ZGA occurs in four- to eight-cell human embryos and in late-two- to four-cell mouse embryos, and is marked by activation of large numbers of genes.[28,29] At this stage, telomere elongation likely depends on the mechanism of ALT,[22] which induces rapid and extensive telomere elongation based on a recombination-like mechanism. To explore whether elongated telomeres were responsible for *DUX4*/*Dux* closure in

mouse embryos, we knocked down *Zscan4*, a gene that occupies a central role in ALT-mediated telomere elongation in embryonic stem cells.[31,32] The small interfering RNA that targeted the homologous region of *Zscan4* was microinjected into zygotes 21–24 h after human chorionic gonadotropin (HCG) administration, effectively reducing *Zscan4* transcripts in the two-cell embryos (Figure S2C). However, we observed that the si*Zscan4*-injected embryos formed normal-looking blastocysts at 96 h post-HCG (Figures S2A and S2B), and they still exhibited telomere elongation, as well as *Dux* closure, at the four-cell stage (Figures S2D and S2E).

Silencing of *Zscan4* did not suppress intrinsic telomere length extension in two- to four-cell embryos, implying that *Zscan4* gene knockdown was insufficient in completely inhibiting ALT during ZGA. Recent studies have shown that the effect of *Zscan4* on ALT in early mouse embryos is not unique, such as the inhibition of LINE-1 gene reverse transcription can also affect the reprogramming of telomeres at the two-cell stage in mouse.[33] We then cultured mouse embryos in the presence of α-amanitin, a blocker of RNA pol II-based transcription that was reported to suppress transcription of a subset of genes in two-cell embryos,[34,35] and acknowledge that *Dux* expression may not be sensitive to α-amanitin treatment.[36] In contrast to the control group, nearly all embryos treated with 25 μg/mL α-amanitin were arrested at the two-cell stage (Figures 2A and 2B). qPCR assay showed that α-amanitin treatment effectively inhibited the activation of numerous early-ZGA genes (Figure S3A), and we noted the failure of telomere elongation and continuous *Dux* expression in late-two-cell-stage embryos with the treatment of 25 μg/mL α-amanitin (Figures 2C–2E). To further determine the function of telomere elongation on *DUX4/Dux* closure, we reduced the concentration of α-amanitin to 1 μg/mL and demonstrated that a fraction of treated embryos were able to develop to the four-cell stage (Figures 2A and 2B). In addition, we noted that treatment with 1 μg/mL α-amanitin led to delayed activation of some early-ZGA genes toward the four-cell stage (Figure S3B). Remarkably, the telomeres of 1 μg/mL α-amanitin-treated four-cell embryos were shorter than their untreated counterparts, and the expression of *Dux* remained at a relatively high level (Figures 2F and 2G). We understand that telomere elongation is a post-replicative event in the cell cycle due to its highly agglutinated heterochromatin structure,[37] whereas the late-two-cell stage entails major ZGA in preimplantation mouse embryos, and that this is followed by silencing of *Dux*. We herein observed that low concentrations of α-amanitin delayed telomere elongation and *Dux* silencing, strengthening the relationship between telomere length and *Dux* expression. In summary, our data revealed that the expression of *DUX4/Dux* required abrogation after the major ZGA process by telomere extension, which was consistent with a previous study in which prolonged expression of Dux led to developmental arrest and embryonic death.[38]

The TPE regulates *DUX4* gene expression by influencing the adjacent heterochromatin state

Human preimplantation embryonic development involves extensive changes to chromatin structure and transcriptional activity. In humans, telomeres and subtelomeres that comprise approximately 500 kb are specialized chromatin structures at the ends of chromosomes,[39] and telomere length-regulated gene expression over close or long distances has been shown to be associated with chromosomal accessibility.[40]

We first utilized our previous LiCAT-seq (low-input chromatin accessibility and transcriptome sequencing) data from human preimplantation embryos[41] to determine whether chromatin accessibility coincided with variations in the telomere length in early embryos. In a previous study, we observed a progressive increase in accessible regions from the two-cell to later embryonic stages, and telomeric or subtelomeric chromatin (100 or 500 kb from the chromosomal terminus) was largely inaccessible (with only 359 peaks detected to the morula stage).[39] The upward trend in telomere accessibility was highest in minor ZGA during early development, with an almost 5-fold increase from 23 peaks at the two-cell stage to 108 peaks in four-cell embryos (Figure 3A). We detected a transient chromatin opening at the minor ZGA stage at the *DUX4* promoter (Figure 3B), suggesting that *DUX4* expression was associated with the accessibility of telomeric regions in ZGA. These results engendered our examination of whether *DUX4* regulation in ZGA was similar to that shown in previous studies of FSHD as reported in a TPE-related manner.[7]

H3K9me3 and H4K20me3 are enriched at telomeres and subtelomeres, and constitute the primary heterochromatin components of telomeres.[42] To investigate the key factors involved in *DUX4* expression, we employed BIX01294 and A-196 to inhibit G9a/GLP and SUV4-20H histone methyltransferase, respectively, in human embryonic stem cells (hESCs),[43] and demonstrated that *DUX4* was significantly augmented upon 2.7 μM BIX01294 treatment for 12 h (Figures S4A–S4C), but that there was no elevation in the A-196 group in

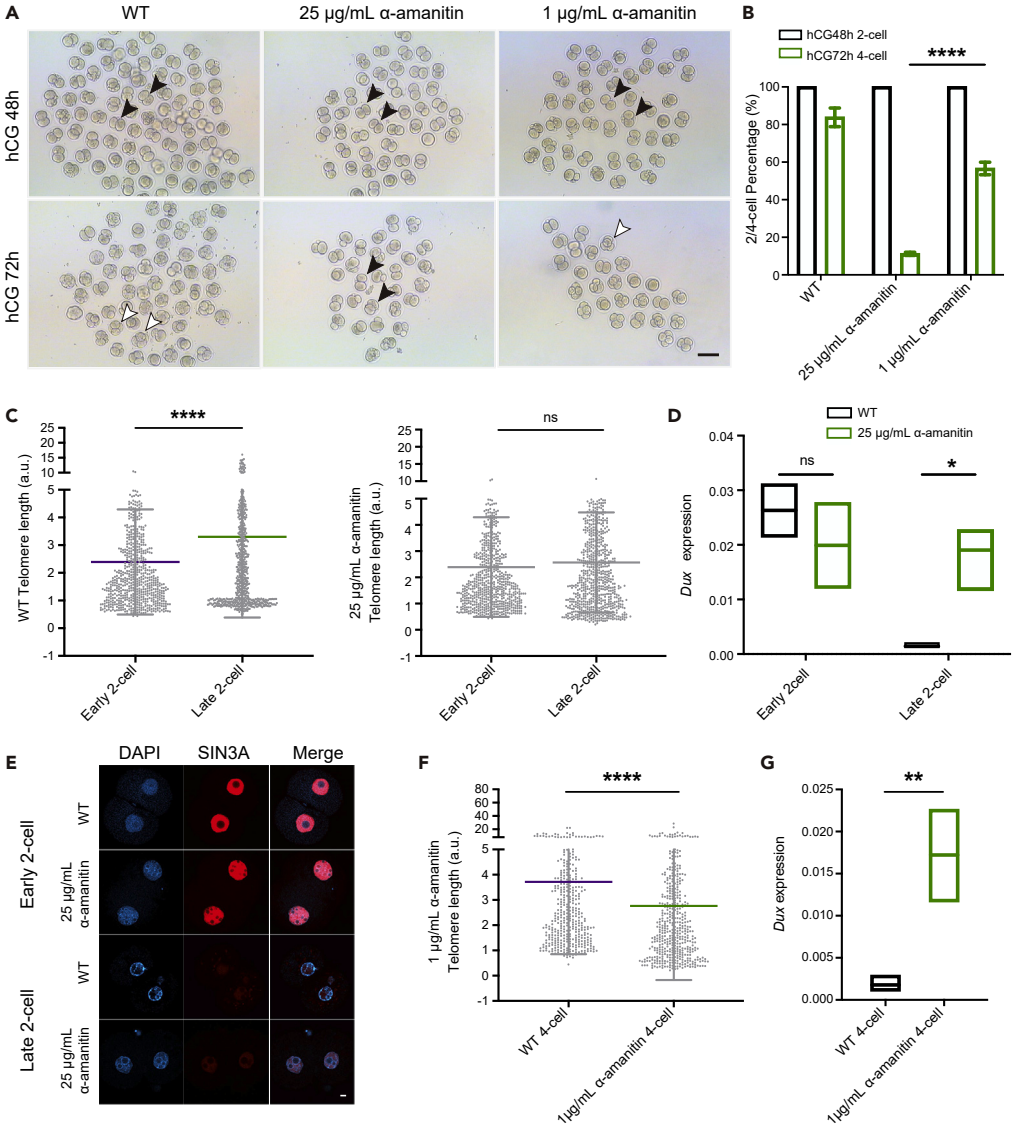

Figure 2. Failure or delay of *DUX4*/*Dux* gene closure due to altered telomere status in early embryos

(A) Representative bright-field images show embryonic development after treatment with α-amanitin (25 and 1 μg/mL). The two- and four-cell embryos (black and white arrows) were harvested *in vivo* at 48 and 72 h post-HCG. The experiment was conducted twice, and at least 80 embryos were analyzed for each experiment (scale bars, 50 μm).

(B) Bar graph shows the percentages of two- and four-cell embryos at 48 and 72 h post-HCG, respectively. Bars represent mean ± SD. Two-tailed unpaired test. ****p< 0.0001.

(C) The telomere length is provided in arbitrary units of fluorescence (a.u.); groups are incubated with or without α-amanitin (25 μg/mL), and each stage contains five embryos. Bars represent mean ± SD. Two-tailed unpaired test. ****p < 0.0001.

(D) *Dux* mRNA expression levels after treatment with α-amanitin (25 μg/mL) in early- and late-two-cell mouse embryos (N = 5, error bars denote mean ± SD). Two-tailed unpaired test. *p < 0.05.

(E) Immunohistochemistry analysis of SIN3A expression during mouse preimplantation development after treatment with 25 μg/mL α-amanitin or not. Differentiation of mouse embryos at early- and late-two-cell stages according to fluorescence intensity; the red signal indicates SIN3A and the blue signal indicates DAPI. The experiment was conducted twice, and at least 15 embryos were analyzed for each experiment (scale bar, 100 μm).

(F) The telomere length is provided in arbitrary units of fluorescence (a.u.) after embryonic treatment with α-amanitin (1 μg/mL), and each embryonic stage contains five embryos. Bars represent mean ± SD. Two-tailed unpaired test. ****p < 0.0001.

(G) *Dux* mRNA expression levels in mouse four-cell embryos after treatment with α-amanitin (1 μg/mL) (N = 5, error bars denote mean ± SD). Two-tailed unpaired test. **p < 0.01.

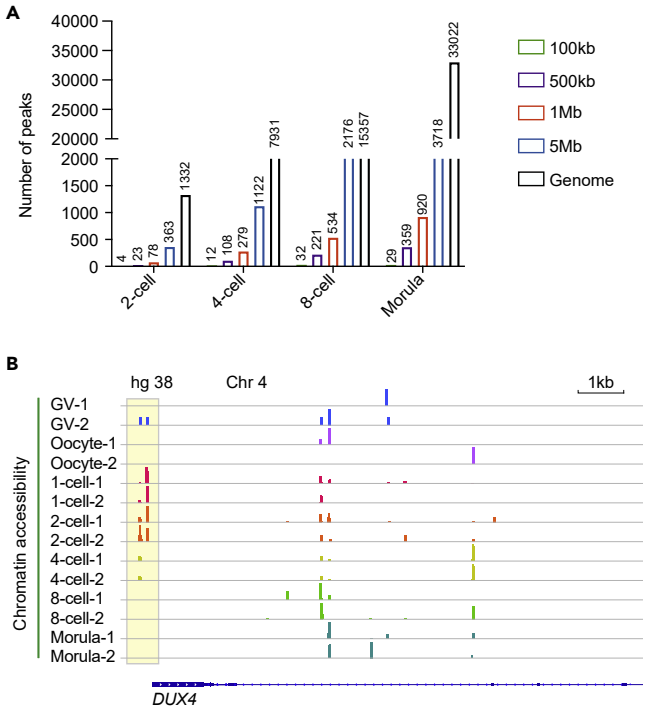

Figure 3. The accessible chromatin landscapes of telomeres from human preimplantation embryos

(A) Number of accessible regions at the indicated developmental stages of human two-cell, four-cell, eight-cell, and morula embryos. Discovered sites included 100 kb, 500 kb, 1 Mb, and 5 Mb from the end of the chromosome and full-length chromosomes by LiCAT-seq.

(B) Genome browser views showing chromatin accessibility around *DUX4*. Stages are germinal vesicle (GV) oocyte; MII oocyte; 2 pronuclear (PN) zygote; and two-cell, four-cell, eight-cell, and morula-stage embryos. Each stage contains two biological samples.

two ESC lines (Figure 4A). Indeed, we ascertained that treatment with BIX01294 from 1 to 3 weeks resulted in telomere elongation, consistent with the fact that reduction of H3K9me3 promoted telomerase-mediated telomere elongation during early embryonic stem cell expansion (Figure S4D).[44] We then focused on H3K9me3 since the spreading and inheritance of heterochromatin are posited to depend on preexisting H3K9me3,[8] and our chromatin immunoprecipitation (ChIP) analysis reflected a reduction in H3K9me3 at the *DUX4* promoter (Figure 4B).

To further investigate the relationships between telomeric chromatin status and *DUX4* expression, we executed CRISPR/Cas9-mediated gene editing near the telomeric region of chromosome 4 to induce telomeric chromatin decompaction at the site of DNA damage.[45] We developed four probes that targeted the end of chromosome 4q and confirmed the successful targeting of telomeric sites by co-localization of TRF2 and DNA damage using immunofluorescence (Figures 4C and 4D). We, in fact, only detected significant upregulation of *DUX4* in the group comprising the 0.5-kb probe (Figure 4E). Subsequent ChIP analysis also revealed attenuated histone methylation of H3K9me3 in the *DUX4* promoter region in this group (Figure 4F), consistent with our speculation that loose telomeric chromatin status favored *DUX4* expression.

The TPE on *DUX4* expression depends on the p53-*DUX4* regulatory axis

Researchers have recently reported that the coupling of the p53 transcription factor to the activation of *DUX4*/*Dux* unifies the developmental regulation of the *Dux* locus in FSHD or in 2CLCs through p53 binding to the subtelomeric long terminal repeat (LTR) 10C element.[46] Analyzing data from the embryonic ZGA process, we found that the level of *p53* mRNA expression showed temporal coherence with *DUX4* (Figures S5C–S5E). To better understand the relationship between H3K9me3 demethylation and *DUX4* transcription, we treated hESCs with doxorubicin (DOX), a chemical that causes double-stranded DNA breaks and can induce *Dux* via a *p*53-binding site in the subtelomeric LTR10C element,[46] in combination with the histone methyltransferase inhibitor BIX01294. In two hESC lines, we observed not only that

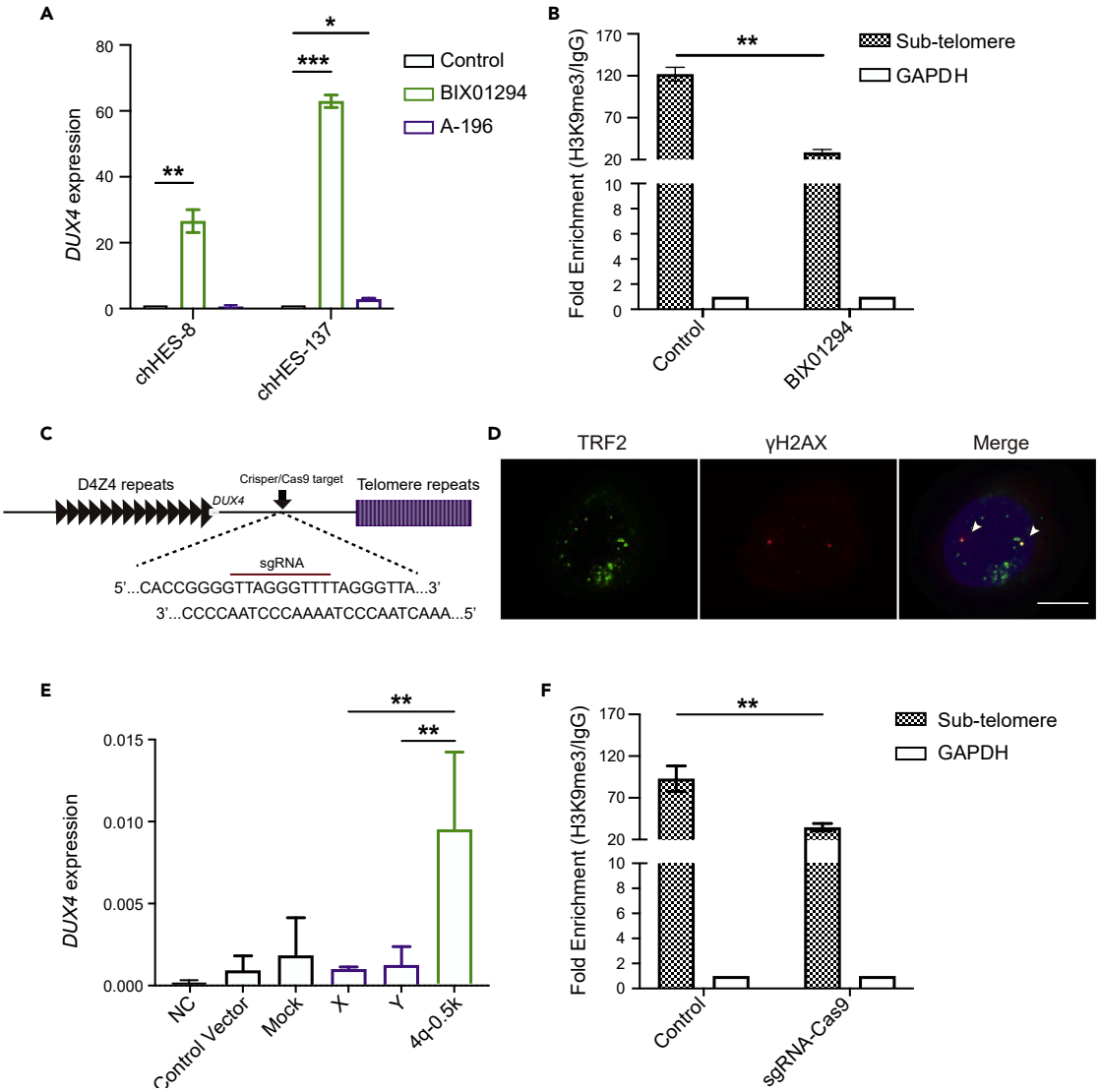

Figure 4. Histone demethylation of telomeres and subtelomeres induces activation of *DUX4*

(A) *DUX4* mRNA expression levels after treatment with the demethylating drugs BIX01294 (2.7 μM) and A-196 (3 μM) in chHES-8 and chHES-137 cells (mean ± SD from three independent experiments). Two-tailed unpaired test. *p < 0.05, **p < 0.01, ***p < 0.001.

(B) ChIP-qPCR analysis of H3K9me3 occupancy at subtelomeres of the Dux promoter region after BIX0294 (2.7 μM) treatment of hESCs. Relative fold-enrichment was normalized to IgG signals, and the GAPDH locus served as a negative control (mean ± SD from three independent experiments). Two-tailed unpaired test. **p < 0.01.

(C) Pattern diagram represents CRISPR/Cas9-processing disposition and effective sequence.

(D) Fluorescence images display TRF2 (green) and γ-H2AX (green) co-localization in hESCs at the indicated passages (scale bar, 10 μm).

(E) *DUX4* mRNA expression levels after DNA damage to the subtelomeric region per CRISPR/Cas9 editing. X and Y chromosomes were used as internal controls (mean ± SD from three independent assays). Two-tailed unpaired test. **p < 0.01.

(F) ChIP-qPCR analysis of H3K9me3 occupancy at subtelomeres of the *Dux* promoter region after CRISPR/Cas9 treatment of hESCs. Relative fold-enrichment was normalized to IgG signals, and the GAPDH locus served as a negative control (mean ± SD from three independent experiments). Two-tailed unpaired test. **p < 0.01.

DOX or BIX01294 induced the expression of *DUX4* but also that the induction was even more pronounced when the two drugs were administered simultaneously (Figure 5A). In addition, we assessed whether the H3K9me3 heterochromatin-related *DUX4*-regulatory pathway was related to the p53-*DUX4* regulatory axis. We used a $p53^{-/-}$ hESC line (chHES-F5) that was derived from the chHES-8 line[47] and treated the cells with BIX1049, DOX, or both drugs (Figures S5A and 5B). Importantly, only the wild-type control hESC line (chHES-8) activated classical DNA damage repair (DDR) genes such as *CDKN1A* and *MDM2* after DOX

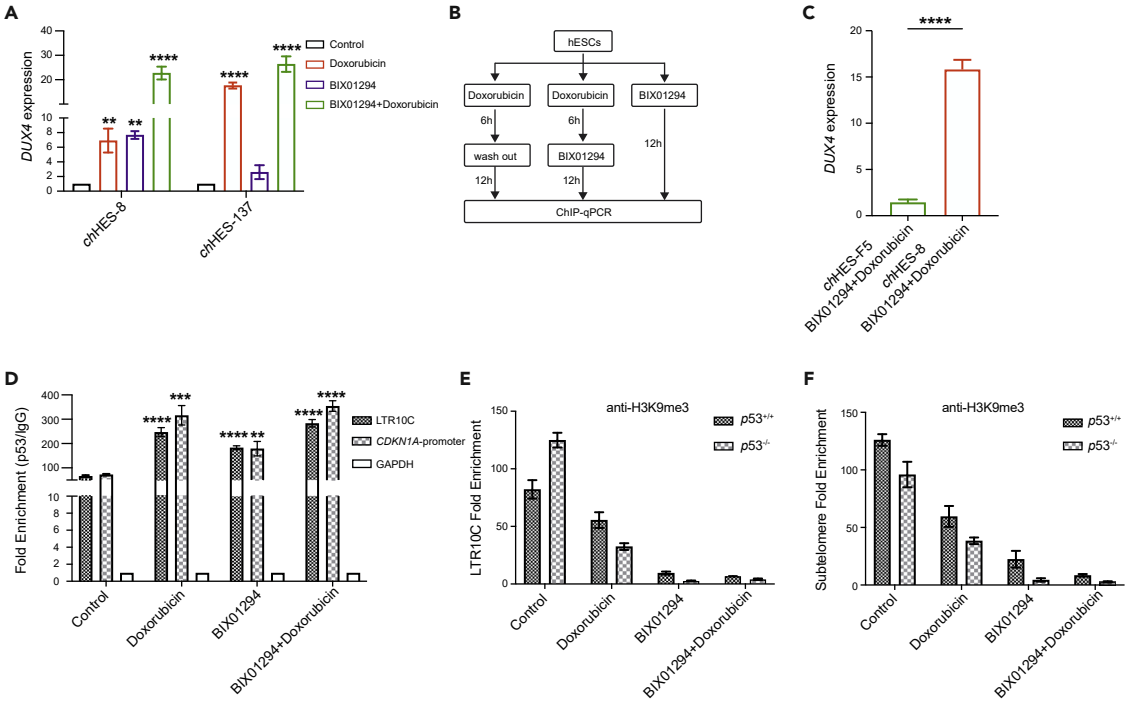

Figure 5. Demethylation of telomeres and binding of p53 to the LTR10C site downstream of *DUX4* constitute important steps in *DUX4* activation

(A) *DUX4* mRNA expression levels in hESC-8 and hESC-137 cell lines after treatment with the demethylating drug BIX01294 (2.7 μM), the DNA-damaging drug doxorubicin (1 μM), or a combination of the two (mean ± SD from three independent assays). Two-tailed unpaired test. **p < 0.01, ****p < 0.0001.

(B) Flowchart illustrates the treatment duration and methodologic sequence via the different drug treatments.

(C) *DUX4* mRNA expression levels in chHES-F5 ($p53^{-/-}$) and chHES-8 ($p53^{+/+}$) cells after treatment with the demethylating drug BIX01294 (2.7 μM) and the DNA-damaging drug doxorubicin (1 μM), (mean ± SD from three independent assays). Two-tailed unpaired test. ****p < 0.0001.

(D) ChIP-qPCR analysis of p53 occupancy at the LTR10C and *CDKN1A* promoter after treatment of $p53^{+/+}$ and $p53^{-/-}$ chHES-8 cell lines with the demethylating agent BIX01294 (2.7 μM), the DNA-damaging agent doxorubicin (1 μM), or the combination of the two drugs. Relative fold-enrichment was normalized to IgG signals, and the GAPDH locus served as a negative control (mean ± SD from three independent assays). Two-tailed unpaired test. **p < 0.01, ***p < 0.001, ****p < 0.0001.

(E) ChIP-qPCR analysis of H3K9me3 occupancy at the LTR10C after treatment of chHES-8 cells with the demethylating agent BIX01294 (2.7 μM), the DNA-damaging agent doxorubicin (1 μM), or the combination of the two. Relative fold-enrichment was normalized to IgG signals, and the GAPDH locus served as a negative control (mean ± SD from three independent assays).

(F) ChIP-qPCR analysis of H3K9me3 occupancy at the subtelomere after treatment of chHES-8 cells with the demethylating agent BIX01294 (2.7 μM), the DNA-damaging agent doxorubicin (1 μM), or the combination of the two. Relative fold-enrichment was normalized to IgG signals, and the GAPDH locus served as a negative control (mean ± SD from three independent assays).

treatment, whereas chHES-F5 did not activate these genes (Figure S5B). In the context of $p53^{-/-}$, there was no significant increase in *DUX4* in any treatment group (Figure 5C). Strikingly, both BIX and DOX treatment resulted in a reduction in H3K9me3 in telomeres and subtelomeres (Figures 5E and 5F), possibly reflecting a potential link between DNA damage and chromatin decondensation. In addition, ChIP analysis revealed increased p53 binding to the LTR10C element in all *DUX4*-enhanced groups (Figure 5D). These data suggest that demethylation of telomeric histones may facilitate transcription-related regulators such as p53 to access binding sites and regulate *DUX4*/*Dux* activation.

DISCUSSION

In the present investigation, we presented an extended characterization of telomere length remodeling in preimplantation embryos and its relationship to ZGA. In both human and mouse embryos, we reliably demonstrated an inverse correlation between the telomere length and expression of the ZGA pioneer factor *DUX4*/*Dux*. In mouse late-two-cell stage embryos, we found that delayed telomere elongation was associated with abnormally continuous *Dux* expression. We also confirmed that the principal mediator of the TPE in affecting the expression of *DUX4* was the H3K9me3 of telomeres and adjacent regions, and that this effect also depended on the accumulation of p53 protein.

We initially demonstrated an integrated variation of the telomere length in human and mouse preimplantation embryos, and in addition to the known extension in the telomere length at the mouse four-cell stage, we also observed that telomeres in early-two-cell embryos were temporarily shortened and then significantly lengthened in the late phase of replication. We thus acknowledge that telomere replication and post-replicative lengthening are events within the late phase of the replication cycle as they belong to a highly agglutinated heterochromatin structure.[37] The lack of sufficient DNA replication time in early zygotes (particularly at the G2/M phase) can lead to the loss of telomere fragments,[48] as can the absence of telomerase and other proteins involved in telomere maintenance in mature oocytes and cleavage embryos,[20] with telomere compensation transpiring during replication from the zygote to the two-cell stage. In late-two-cell embryos, the recombination-mediated telomeric mechanism and translation of related genes such as *Zscan4* may explain the rapid elongation of telomeres.[22] The telomere length of human preimplantation embryos was noted to change across different developmental stages, such that the telomeres in blastocysts were significantly longer than those at cleavage stages.[20] However, it is necessary to achieve and record a specific number of successive time points to exclude individual differences and thus better clarify the feature of human telomere variation during early embryonic development. We determined the telomere length in a large number of embryos and established a continuous model of the telomere length in human preimplantation embryos, with our results revealing that telomeres remained truncated before the four-cell stage and subsequently increased in length rapidly from the eight-cell stage, which was similar to the case for two- to four-cell mouse embryos. In conjunction with previous observations of ALT-associated PML bodies (APB bodies, components of promyelocytic leukemia bodies, and telomere DNA co-localization markers of ALT) in early embryos and increased mRNAs for genes related to telomere recombination,[49] we hypothesize that ALT-dependent telomere lengthening patterns exist in human ZGA.

In mouse embryonic stem cell expansion, telomere erosion leads to 2CLC transformation that can be induced by *Dux*.[5] When we added *α*-amanitin to mouse embryos,[34,50] the cells failed to pass through the two-cell stage and to extend telomeres, whereas the *Dux* gene was continuously expressed into the late-two-cell and even into the four-cell stages. These experimental results strengthened the hypothetical relationship between embryonic telomere length and the activation of *Dux*. Several lines of evidence suggest that *DUX4*/*Dux* activation is conserved in mammalian ZGA. Unlike the human *DUX4* gene, the mouse *Dux* gene is not located in the subtelomeric region, and the specific pattern of the TPE might therefore be different. Two forms of TPE are known, classical TPE and TPE over long distance (TPE-OLD): classical TPE follows the classical model of continuous heterochromatin spreading in which TPE declines with distance from the telomere, whereas TPE-OLD shows a novel mechanism that involves the physical association of the telomere by loops to chromatin near these genes. TPE-OLD genes are generally repressed in cells with long telomeres—with chromosomal loops occurring between the loci of these genes and their respective telomere ends—and these genes are regulated by telomere length-dependent loops.[40] It is noteworthy that the telomere length in mice is much longer than that in humans (approximately 70 kb versus 10 kb),[51,52] potentially producing a wider spatial impact. Telomere shortening leads to the loss of the heterochromatic properties of telomeres and subtelomeres, and abrogates the inhibition of TPE on target gene expression.[16,53,54] Although ATAC-seq (assay for transposase-accessible chromatin using sequencing) also revealed that *DUX4* availability in human embryos was consistent with the telomere length, more evidence is still needed to fully explain the mechanism underlying the TPE on *DUX4*/*Dux*.

Telomeric reconstruction occurs during embryonic stem cell line generation, during the reprogramming of induced pluripotent stem cells, and during 2C-like transformation in mouse ESCs; it is associated with genomic stability and bona fide self-renewal.[55] Embryonic omics change dramatically in ZGA, and cells acquire totipotency/pluripotency. We herein provided detailed data on changes in the telomere length during ZGA in human and mouse preimplantation embryos, explored the possibility that the TPE affects the regulation of *DUX4*/*Dux* gene expression in embryos, and suggest that telomere chromatin remodeling is involved in the ZGA process.

Limitations of the study

Despite carrying out considerable experimental validation, there are some limitations to our study. Since the mouse Dux gene is not located at the end of the chromosome, the classical TPE pathway may not explain its activation mechanism in early embryonic development and TPE-OLD may be a potential pathway that we discussed in the article. However, this difference still requires further confirmation in mouse embryonic development. In addition, a more direct examination of the causal relationship between

telomeres and *DUX4*/*Dux* in early ZGA is still necessary. Although we have already answered some of the questions in human embryonic stem cells and the available ATAC sequencing data from embryos, 3D analysis as presented by Hi-C may be able to make a greater breakthrough in confirming the relationship between the two.

STAR★METHODS

Detailed methods are provided in the online version of this paper and include the following:

- KEY RESOURCES TABLE
- RESOURCE AVAILABILITY
  - Lead contact
  - Materials availability
  - Data and code availability
- EXPERIMENTAL MODEL AND SUBJECT DETAILS
  - Patients
  - Collection of human material
  - Animals and collection of mouse embryos
  - Cell culture
- METHOD DETAILS
  - Immunofluorescence microscopy
  - Telomere Q-FISH
  - Telomere measurement by quantitative PCR
  - Single-oocyte and embryonic quantitative reverse-transcription PCR (RT-qPCR)
  - Total RNA isolation, reverse transcription, and quantitative PCR
  - Western blot analysis
  - CRISPR/Cas9
  - Chromatin immunoprecipitation assay
  - Microinjection of small interfering RNAs (siRNAs) and embryo culture
- QUANTIFICATION AND STATISTICAL ANALYSIS

SUPPLEMENTAL INFORMATION

Supplemental information can be found online at https://doi.org/10.1016/j.isci.2023.106158.

ACKNOWLEDGMENTS

We thank all staff at Hunan Guangxiu Hospital and the Reproductive and Genetic Hospital of CITIC-Xiangya. This work was supported by the National Natural Science Foundation of China (grant nos. 81974230 and 82001556) and the Natural Science Foundation of Hunan Province (grant no. 2019JJ50397). We thank LetPub (www.letpub.com) for its linguistic assistance during the preparation of this manuscript.

AUTHOR CONTRIBUTIONS

S.Z., L.L., and G.L. conceived the project; X.Z., and C.Z. designed the experiments, conducted most of the experiments and analyzed the data; Q.Z. microinjected mRNAs or siRNAs into mouse oocytes; F.M. analyzed the RNA-seq data and constructed libraries of single-cell RNA-seq; D.Z. and Q.Y. assisted in designing CRISPR sgRNAs; T.Z., X.C., and J.R. assisted with human embryo-related experiments; S.Z. and X.Z. wrote the draft of the manuscript, with contributions and approval from all authors; and S.Z., L.L., and G.L. critically revised the manuscript. All authors read and approved the final manuscript.

DECLARATION OF INTERESTS

The authors declare no competing interests.

INCLUSION AND DIVERSITY

We support inclusive, diverse, and equitable conduct of research.

Received: September 16, 2022
Revised: November 3, 2022
Accepted: February 3, 2023
Published: February 8, 2023

REFERENCES

1. Pálfy, M., Joseph, S.R., and Vastenhouw, N.L. (2017). The timing of zygotic genome activation. Curr. Opin. Genet. Dev. *43*, 53–60. https://doi.org/10.1016/j.gde.2016.12.001.

2. Ko, M.S.H. (2016). Zygotic genome activation revisited: looking through the expression and function of Zscan4. Curr. Top. Dev. Biol. *120*, 103–124. https://doi.org/10.1016/bs.ctdb.2016.04.004.

3. Schulz, K.N., and Harrison, M.M. (2019). Mechanisms regulating zygotic genome activation. Nat. Rev. Genet. *20*, 221–234. https://doi.org/10.1038/s41576-018-0087-x.

4. De Iaco, A., Planet, E., Coluccio, A., Verp, S., Duc, J., and Trono, D. (2017). DUX-family transcription factors regulate zygotic genome activation in placental mammals. Nat. Genet. *49*, 941–945. https://doi.org/10.1038/ng.3858.

5. Hendrickson, P.G., Doráis, J.A., Grow, E.J., Whiddon, J.L., Lim, J.W., Wike, C.L., Weaver, B.D., Pflueger, C., Emery, B.R., Wilcox, A.L., et al. (2017). Conserved roles of mouse DUX and human DUX4 in activating cleavage-stage genes and MERVL/HERVL retrotransposons. Nat. Genet. *49*, 925–934. https://doi.org/10.1038/ng.3844.

6. Wang, L.H., and Tawil, R. (2016). Facioscapulohumeral dystrophy. Curr. Neurol. Neurosci. Rep. *16*, 66. https://doi.org/10.1007/s11910-016-0667-0.

7. Stadler, G., Rahimov, F., King, O.D., Chen, J.C.J., Robin, J.D., Wagner, K.R., Shay, J.W., Emerson, C.P., Jr., and Wright, W.E. (2013). Telomere position effect regulates DUX4 in human facioscapulohumeral muscular dystrophy. Nat. Struct. Mol. Biol. *20*, 671–678. https://doi.org/10.1038/nsmb.2571.

8. Cutter DiPiazza, A.R., Taneja, N., Dhakshnamoorthy, J., Wheeler, D., Holla, S., and Grewal, S.I.S. (2021). Spreading and epigenetic inheritance of heterochromatin require a critical density of histone H3 lysine 9 tri-methylation. Proc. Natl. Acad. Sci. USA *118*. e2100699118. https://doi.org/10.1073/pnas.2100699118.

9. Baur, J.A., Zou, Y., Shay, J.W., and Wright, W.E. (2001). Telomere position effect in human cells. Science *292*, 2075–2077. https://doi.org/10.1126/science.1062329.

10. Decottignies, A. (2014). The telomere position effect: silence in the back row! Med. Sci. *30*, 173–178. https://doi.org/10.1051/medsci/20143002015.

11. Weuts, A., Voet, T., Verbeeck, J., Lambrechts, N., Wirix, E., Schoonjans, L., Danloy, S., Marynen, P., and Froyen, G. (2012). Telomere length homeostasis and telomere position effect on a linear human artificial chromosome are dictated by the genetic background. Nucleic Acids Res. *40*, 11477–11489. https://doi.org/10.1093/nar/gks926.

12. Schoeftner, S., and Blasco, M.A. (2010). Chromatin regulation and non-coding RNAs at mammalian telomeres. Semin. Cell Dev. Biol. *21*, 186–193. https://doi.org/10.1016/j.semcdb.2009.09.015.

13. Thakur, J., Packiaraj, J., and Henikoff, S. (2021). Sequence, chromatin and evolution of satellite DNA. Int. J. Mol. Sci. *22*, 4309. https://doi.org/10.3390/ijms22094309.

14. Udugama, M., M Chang, F.T., Chan, F.L., Tang, M.C., Pickett, H.A., McGhie, J.D.R., Mayne, L., Collas, P., Mann, J.R., and Wong, L.H. (2015). Histone variant H3.3 provides the heterochromatic H3 lysine 9 tri-methylation mark at telomeres. Nucleic Acids Res. *43*, 10227–10237. https://doi.org/10.1093/nar/gkv847.

15. Marion, R.M., Strati, K., Li, H., Tejera, A., Schoeftner, S., Ortega, S., Serrano, M., and Blasco, M.A. (2009). Telomeres acquire embryonic stem cell characteristics in induced pluripotent stem cells. Cell Stem Cell *4*, 141–154. https://doi.org/10.1016/j.stem.2008.12.010.

16. Kim, W., and Shay, J.W. (2018). Long-range telomere regulation of gene expression: telomere looping and telomere position effect over long distances (TPE-OLD). Differentiation. *99*, 1–9. https://doi.org/10.1016/j.diff.2017.11.005.

17. Ottaviani, A., Gilson, E., and Magdinier, F. (2008). Telomeric position effect: from the yeast paradigm to human pathologies? Biochimie *90*, 93–107. https://doi.org/10.1016/j.biochi.2007.07.022.

18. Smith, E.M., Pendlebury, D.F., and Nandakumar, J. (2020). Structural biology of telomeres and telomerase. Cell. Mol. Life Sci. *77*, 61–79. https://doi.org/10.1007/s00018-019-03369-x.

19. Keefe, D.L. (2020). Telomeres and genomic instability during early development. Eur. J. Med. Genet. *63*, 103638. https://doi.org/10.1016/j.ejmg.2019.03.002.

20. Ozturk, S., Sozen, B., and Demir, N. (2014). Telomere length and telomerase activity during oocyte maturation and early embryo development in mammalian species. Mol. Hum. Reprod. *20*, 15–30. https://doi.org/10.1093/molehr/gat055.

21. Huang, J., Wang, F., Okuka, M., Liu, N., Ji, G., Ye, X., Zuo, B., Li, M., Liang, P., Ge, W.W., et al. (2011). Association of telomere length with authentic pluripotency of ES/iPS cells. Cell Res. *21*, 779–792. https://doi.org/10.1038/cr.2011.16.

22. Liu, L., Bailey, S.M., Okuka, M., Muñoz, P., Li, C., Zhou, L., Wu, C., Czerwiec, E., Sandler, L., Seyfang, A., et al. (2007). Telomere lengthening early in development. Nat. Cell Biol. *9*, 1436–1441. https://doi.org/10.1038/ncb1664.

23. Schaetzlein, S., Lucas-Hahn, A., Lemme, E., Kues, W.A., Dorsch, M., Manns, M.P., Niemann, H., and Rudolph, K.L. (2004). Telomere length is reset during early mammalian embryogenesis. Proc. Natl. Acad. Sci. USA *101*, 8034–8038. https://doi.org/10.1073/pnas.0402400101.

24. Burton, A., and Torres-Padilla, M.E. (2014). Chromatin dynamics in the regulation of cell fate allocation during early embryogenesis. Nat. Rev. Mol. Cell Biol. *15*, 723–734. https://doi.org/10.1038/nrm3885.

25. Eckersley-Maslin, M.A., Alda-Catalinas, C., and Reik, W. (2018). Dynamics of the epigenetic landscape during the maternal-to-zygotic transition. Nat. Rev. Mol. Cell Biol. *19*, 436–450. https://doi.org/10.1038/s41580-018-0008-z.

26. Jimenez, R., Melo, E.O., Davydenko, O., Ma, J., Mainigi, M., Franke, V., and Schultz, R.M. (2015). Maternal SIN3A regulates reprogramming of gene expression during mouse preimplantation development. Biol. Reprod. *93*, 89. https://doi.org/10.1095/biolreprod.115.133504.

27. He, C., Jing, S., Dai, C., Tu, C., Tan, Z., Du, J., Lu, G.X., Lin, G., and Zeng, S. (2019). Telomerase insufficiency induced telomere erosion accumulation in successive generations in dyskeratosis congenita family. Mol. Genet. Genomic Med. *7*, e00709. https://doi.org/10.1002/mgg3.709.

28. Leng, L., Sun, J., Huang, J., Gong, F., Yang, L., Zhang, S., Yuan, X., Fang, F., Xu, X., Luo, Y., et al. (2019). Single-cell transcriptome analysis of uniparental embryos reveals parent-of-origin effects on human preimplantation development. Cell Stem Cell *25*, 697–712.e6. https://doi.org/10.1016/j.stem.2019.09.004.

29. Yan, L., Yang, M., Guo, H., Yang, L., Wu, J., Li, R., Liu, P., Lian, Y., Zheng, X., Yan, J., et al. (2013). Single-cell RNA-Seq profiling of human preimplantation embryos and embryonic stem cells. Nat. Struct. Mol. Biol. *20*, 1131–1139. https://doi.org/10.1038/nsmb.2660.

30. Chen, Z., and Zhang, Y. (2019). Loss of DUX causes minor defects in zygotic genome activation and is compatible with mouse development. Nat. Genet. *51*, 947–951. https://doi.org/10.1038/s41588-019-0418-7.

31. Le, R., Huang, Y., Zhang, Y., Wang, H., Lin, J., Dong, Y., Li, Z., Guo, M., Kou, X., Zhao, Y.,

et al. (2021). Dcaf11 activates Zscan4-mediated alternative telomere lengthening in early embryos and embryonic stem cells. Cell Stem Cell *28*, 732–747.e9. https://doi.org/10.1016/j.stem.2020.11.018.

32. Zalzman, M., Falco, G., Sharova, L.V., Nishiyama, A., Thomas, M., Lee, S.L., Stagg, C.A., Hoang, H.G., Yang, H.T., Indig, F.E., et al. (2010). Zscan4 regulates telomere elongation and genomic stability in ES cells. Nature *464*, 858–863. https://doi.org/10.1038/nature08882.

33. Wang, F., Chamani, I.J., Luo, D., Chan, K., Navarro, P.A., and Keefe, D.L. (2021). Inhibition of LINE-1 retrotransposition represses telomere reprogramming during mouse 2-cell embryo development. J. Assist. Reprod. Genet. *38*, 3145–3153. https://doi.org/10.1007/s10815-021-02331-w.

34. Davis, W., Jr., De Sousa, P.A., and Schultz, R.M. (1996). Transient expression of translation initiation factor eIF-4C during the 2-cell stage of the preimplantation mouse embryo: identification by mRNA differential display and the role of DNA replication in zygotic gene activation. Dev. Biol. *174*, 190–201. https://doi.org/10.1006/dbio.1996.0065.

35. Jin, X.L., and O'Neill, C. (2014). The regulation of the expression and activation of the essential ATF1 transcription factor in the mouse preimplantation embryo. Reproduction *148*, 147–157. https://doi.org/10.1530/REP-13-0535.

36. Zeng, F., and Schultz, R.M. (2005). RNA transcript profiling during zygotic gene activation in the preimplantation mouse embryo. Dev. Biol. *283*, 40–57. https://doi.org/10.1016/j.ydbio.2005.03.038.

37. Doksani, Y. (2019). The response to DNA damage at telomeric repeats and its consequences for telomere function. Genes *10*, 318. https://doi.org/10.3390/genes10040318.

38. Guo, M., Zhang, Y., Zhou, J., Bi, Y., Xu, J., Xu, C., Kou, X., Zhao, Y., Li, Y., Tu, Z., et al. (2019). Precise temporal regulation of Dux is important for embryo development. Cell Res. *29*, 956–959. https://doi.org/10.1038/s41422-019-0238-4.

39. Mefford, H.C., and Trask, B.J. (2002). The complex structure and dynamic evolution of human subtelomeres. Nat. Rev. Genet. *3*, 91–102. https://doi.org/10.1038/nrg727.

40. Robin, J.D., Ludlow, A.T., Batten, K., Magdinier, F., Stadler, G., Wagner, K.R., Shay, J.W., and Wright, W.E. (2014). Telomere position effect: regulation of gene expression with progressive telomere shortening over long distances. Genes Dev. *28*, 2464–2476. https://doi.org/10.1101/gad.251041.114.

41. Liu, L., Leng, L., Liu, C., Lu, C., Yuan, Y., Wu, L., Gong, F., Zhang, S., Wei, X., Wang, M., et al. (2019). An integrated chromatin accessibility and transcriptome landscape of human pre-implantation embryos. Nat. Commun. *10*, 364. https://doi.org/10.1038/s41467-018-08244-0.

42. Allshire, R.C., and Madhani, H.D. (2018). Ten principles of heterochromatin formation and function. Nat. Rev. Mol. Cell Biol. *19*, 229–244. https://doi.org/10.1038/nrm.2017.119.

43. Dworak, N., Makosa, D., Chatterjee, M., Jividen, K., Yang, C.S., Snow, C., Simke, W.C., Johnson, I.G., Kelley, J.B., and Paschal, B.M. (2019). A nuclear lamina-chromatin-Ran GTPase axis modulates nuclear import and DNA damage signaling. Aging Cell *18*, e12851. https://doi.org/10.1111/acel.12851.

44. Zeng, S., Liu, L., Sun, Y., Xie, P., Hu, L., Yuan, D., Chen, D., Ouyang, Q., Lin, G., and Lu, G. (2014). Telomerase-mediated telomere elongation from human blastocysts to embryonic stem cells. J. Cell Sci. *127*, 752–762. https://doi.org/10.1242/jcs.131433.

45. Chagin, V.O., Reinhart, B., Becker, A., Mortusewicz, O., Jost, K.L., Rapp, A., Leonhardt, H., and Cardoso, M.C. (2019). Processive DNA synthesis is associated with localized decompaction of constitutive heterochromatin at the sites of DNA replication and repair. Nucleus *10*, 231–253. https://doi.org/10.1080/19491034.2019.1688932.

46. Grow, E.J., Weaver, B.D., Smith, C.M., Guo, J., Stein, P., Shadle, S.C., Hendrickson, P.G., Johnson, N.E., Butterfield, R.J., Menafra, R., et al. (2021). p53 convergently activates Dux/DUX4 in embryonic stem cells and in facioscapulohumeral muscular dystrophy cell models. Nat. Genet. *53*, 1207–1220. https://doi.org/10.1038/s41588-021-00893-0.

47. Li, Y., Huang, C., Zha, L., Kong, M., Yang, Q., Zhu, Y., Peng, Y., Ouyang, Q., Lu, G., Lin, G., and Zhou, D. (2019). Generation of NERCe003-A-3, a p53 compound heterozygous mutation human embryonic stem cell line, by CRISPR/Cas9 editing. Stem Cell Res. *34*, 101371. https://doi.org/10.1016/j.scr.2018.101371.

48. Benetti, R., García-Cao, M., and Blasco, M.A. (2007). Telomere length regulates the epigenetic status of mammalian telomeres and subtelomeres. Nat. Genet. *39*, 243–250. https://doi.org/10.1038/ng1952.

49. Chang, F.T.M., McGhie, J.D., Chan, F.L., Tang, M.C., Anderson, M.A., Mann, J.R., Andy Choo, K.H., and Wong, L.H. (2013). PML bodies provide an important platform for the maintenance of telomeric chromatin integrity in embryonic stem cells. Nucleic Acids Res. *41*, 4447–4458. https://doi.org/10.1093/nar/gkt114.

50. Uh, K., and Lee, K. (2017). Use of chemicals to inhibit DNA replication, transcription, and protein synthesis to study zygotic genome activation. Methods Mol. Biol. *1605*, 191–205. https://doi.org/10.1007/978-1-4939-6988-3_13.

51. de Lange, T. (2009). How telomeres solve the end-protection problem. Science *326*, 948–952. https://doi.org/10.1126/science.1170633.

52. Martens, U.M., Chavez, E.A., Poon, S.S., Schmoor, C., and Lansdorp, P.M. (2000). Accumulation of short telomeres in human fibroblasts prior to replicative senescence. Exp. Cell Res. *256*, 291–299. https://doi.org/10.1006/excr.2000.4823.

53. Blasco, M.A. (2005). Telomeres and human disease: ageing, cancer and beyond. Nat. Rev. Genet. *6*, 611–622. https://doi.org/10.1038/nrg1656.

54. Blasco, M.A. (2007). The epigenetic regulation of mammalian telomeres. Nat. Rev. Genet. *8*, 299–309. https://doi.org/10.1038/nrg2047.

55. Simpson, J.L., and Wells, D. (2014). Telomere length and aneuploidy: clinical and biological insights into human preimplantation embryos. Reprod. Biomed. Online *28*, 531–532. https://doi.org/10.1016/j.rbmo.2014.03.009.

56. He, C., Zhang, X., Li, J., Dai, C., Wang, S., Dai, C., and Zeng, S. (2022). Low-dose telomerase is required for the expansion and migration of placental mesenchymal stem cells. Biochem. Biophys. Res. Commun. *636*, 40–47. https://doi.org/10.1016/j.bbrc.2022.10.093.

57. Drost, J., van Jaarsveld, R.H., Ponsioen, B., Zimberlin, C., van Boxtel, R., Buijs, A., Sachs, N., Overmeer, R.M., Offerhaus, G.J., Begthel, H., et al. (2015). Sequential cancer mutations in cultured human intestinal stem cells. Nature *521*, 43–47. https://doi.org/10.1038/nature14415.

STAR★METHODS

KEY RESOURCES TABLE

REAGENT or RESOURCE	SOURCE	IDENTIFIER
Antibodies		
Rabbit anti-mSin3A	Abcam	Cat # 3479
Mouse anti-γH2AX	Cell Signaling Technology	Cat # 80312
Rabbit anti-H3K9me3	Cell Signaling Technology	Cat # 13969
Rabbit anti-TRF2	Abcam	Cat # ab108997
p53 Rabbit pAb	ABclonal	Cat # A0263
Alexa Fluor 594 donkey anti-goat IgG	Thermo Fisher Scientific	Cat # A-11058
Alexa Fluor 488 donkey anti-rabbit IgG	Thermo Fisher Scientific	Cat # A-21206
p53 Antibody (DO-1)	Santa Cruz	Cat # sc-126
Anti-Vinculin antibody	Abcam	Cat # ab155120
goat anti-mouse IgG-HRP	Santa Cruz	Cat # sc-2005
Chemicals, peptides, and recombinant proteins		
BIX01294	Selleck	Cat # S8006
Doxorubicin (Adriamycin) HCl	Selleck	Cat # S1208
A-196	Selleck	Cat # S7983
DAPI (4′,6-Diamidino-2-Phenylindole, Dilactate)	Thermo Fisher Scientific	Cat # D3571
Bovine serum albumin, fraction V, heat shock isolation	BBI	Cat # A600332-0100
Tween 20	Sigma-Aldrich	Cat # 9005-64-5
Triton X-100	Sigma-Aldrich	Cat # T8787
4% Paraformaldehyde Fix Solution	Sangon Biotech	Cat # E672002
Accutase	Sigma-Aldrich	Cat # A6964
DPBS	Sigma-Aldrich	Cat # TMS-012
Rock inhibitor Y27632	Calbiochem	Cat # 688002
TRIzol Reagent	Thermo Fisher Scientific	Cat # 15596018
Alpha-amanitin	APExBIO	Cat # A4548
FBS	Hyclone	Cat # SH30370.03
SYBR Green Master Mix	Roche	Cat # 4913914001
DNase/RNase-free ddH2O	Absin	Cat # abs9259
Matrigel	Corning	Cat # 354234
Anhydrous ethanol	Fuyugs	Cat # 64-17-5
Trichloromethane	Fuyugs	Cat # 67-66-3
2-propanol	Fuyugs	Cat # 67-63-0
SuperSignal West Femto	Thermo Fisher Scientific	Cat # 34096
RIPA Lysis Buffer	Cwbio	Cat # CW2333
Stripping Buffer	Cwbio	Cat # CW0056
Opti-MEM	Thermo Fisher Scientific	Cat # 31985070
mTeSR Plus	STEMCELL Technologies	Cat # 05850
HCG	Livzon	Cat # H44020673
PMSG	Cen's	Cat # 110204564
G-1 Plus	Vitrolife	Cat # 10127
Advanced DMEM/F-12	Gibco	Cat # 12634010

(*Continued on next page*)

Continued

REAGENT or RESOURCE	SOURCE	IDENTIFIER
Tyrode's	Sigma-Aldrich	Cat # T1788
EZ-Buffers H 10X TBST Buffer	Sangon Biotech	Cat # C520009
Critical commercial assays		
Magna ChIP™ A/G Chromatin Immunoprecipitation Kit	Mecrk	Cat # 17-10085
Transcriptor First Strand cDNA Synthesis Kit	Roche	Cat # 04896866001
QIAamp DNA Mini kit	Qiagen	Cat # 56404
SuperScript II reverse transcriptase	Invitrogen	Cat # 18064071
Agencourt AMPure XP Reagent	Beckman Coulter	Cat # A63881
Nuclear and Cytoplasmic Extraction Kit	Cwbio	Cat # CW0199
Lipofectamine 2000	Invitrogen	Cat # 11668-019
Experimental models: Cell lines		
Human embryonic stem cells:chHES-8, chHES-8 P53−/−, chHES-90, chHES-137	National engineering research center of human stem cells, Changsha, China.	Zeng et al.[44]
Human:TERT$^{-/-}$ MSC	National engineering research center of human stem cells, Changsha, China.	He et al.[56]
Human: HEK-293	National engineering research center of human stem cells, Changsha, China.	N/A
L-5178Y-S	National engineering research center of human stem cells, Changsha,China	N/A
Oligonucleotides		
Telo C PNA probe	PNA Bio	N/A
Telo G PNA probe	PNA Bio	N/A
qPCR, *GAPDH* Forward	GAAGGTGAAGGTCGGAGTC	N/A
qPCR, *GAPDH* Reverse	GAAGATGGTGATGGGATTTC	N/A
qPCR, *DUX4* Forward	CTGGTCTTCTACGTGGAAATGAA	N/A
qPCR, *DUX4* Reverse	CGTGGGAGTCTTGAGTGTGC	N/A
qPCR, *ZSCAN4* Forward	TTTCAGTGTGAACCATCCGAG	N/A
qPCR, *ZSCAN4* Reverse	AGCACCATTCTTGAGAACTCAG	N/A
qPCR, *LEUTX* Forward	GCTACAATGGGGAAACTGGC	N/A
qPCR, *LEUTX* Reverse	CTCTTCCATTTGGCACGCTG	N/A
qPCR, *KLF17* Forward	GTCTAGACCCCACCCAGTCT	N/A
qPCR, *KLF17* Reverse	GAGTTCTCGTTATCCTGGGCA	N/A
qPCR, *CDKN1A* Forward	GCTGCCGAAGTCAGTTCCT	N/A
qPCR, *CDKN1A* Reverse	TTCTGACATGGCGCCTCCT	N/A
qPCR, *MDM2* Forward	AGGAGATTTGTTTGGCGTGC	N/A
qPCR, *MDM2* Reverse	TGAGTCCGATGATTCCTGCTG	N/A
qPCR, *BCL-2* Forward	ATGTGTGTGGAGAGCGTCAA	N/A
qPCR, *BCL-2* Reverse	GGGCCGTACAGTTCCACAAA	N/A
qPCR, *mGapdh* Forward	GGTTGTCTCCTGCGACTTCA	N/A
qPCR, *mGapdh* Reverse	TGGTCCAGGGTTTCTTACTCC	N/A
qPCR, *mDux* Forward	GCCCTGCTATCAACTTTCAAGA	N/A
qPCR, *mDux* Reverse	TCCTCTCCACTGCGATTCCT	N/A
qPCR, *mZscan4* Forward	GATTATTGGCCACAGGACAAG	N/A
qPCR, *mZscan4* Reverse	TCAGGGTGCTGTTCTTTCTG	N/A
qPCR, *mLeutx* Forward	GACGACCAGATCCCAACA	N/A

(*Continued on next page*)

Continued

REAGENT or RESOURCE	SOURCE	IDENTIFIER
qPCR, *mLeutx* Reverse	CAAGGCATAGTCTTCCAGTAG	N/A
qPCR, *mSlc34a2* Forward	AGTTCACTCCAGATCGCCCT	N/A
qPCR, *mSlc34a2* Reverse	CCAGCGATACTTGGCAGAGA	N/A
qPCR, *mDcaf11* Forward	GCCGGGGACTTTGATAGGATT	N/A
qPCR, *mDcaf11* Reverse	CAGAAACGGGGCAGAAGCTA	N/A
qPCR, *mTdpoz3* Forward	TCTCCAATGTCCAATGCTTTCTG	N/A
qPCR, *mTdpoz3* Reverse	ACGGTTCCAACTATGCTCACC	N/A
qPCR, *mWdr74* Forward	AAGAGCCCAACCAAGTACCCT	N/A
qPCR, *mWdr74* Reverse	CTTCCTTCTTTGGAGAGCACCT	N/A
qPCR, *mZfp352* Forward	AGAGGACAAGACCCAGTGCAG	N/A
qPCR, *mZfp352* Reverse	GAGGTCCTCATCTGACCCAAG	N/A
qPCR, *mEif1a* Forward	AACAGGCGCAGAGGTAAAAA	N/A
qPCR, *mEif1a* Reverse	GCACAGCCTCCTTACACCAT	N/A
qPCR, *mZfp622* Forward	TTCCGATGATGGATTGGAATGTG	N/A
qPCR, *mZfp622* Reverse	GCTTGAATGATGGGAGCAAAAC	N/A
qPCR, *mDuxbl* Forward	GCAGGCCAACCTCAAACAG	N/A
qPCR, *mDuxbl* Reverse	CGCAGGGCTCTCCTAAATCTT	N/A
qPCR, *mTdpoz4* Forward	CACACCAGCCCTTTGGATTCG	N/A
qPCR, *mTdpoz4* Reverse	TGGAGTACGCTCACCTTGCAG	N/A
qPCR, *mSp110* Forward	GCACAGCACGAAGAACCACAC	N/A
qPCR, *mSp110* Reverse	GGCCTTACCACAGGTCACAG	N/A
ChIP-qPCR, *CDKN1A*-promoter Forward	AGCAGGCTGTGGCTCTGATT	N/A
ChIP-qPCR, *CDKN1A*-promoter Reverse	CAAAATAGCCACCAGCCTCTTCT	N/A
ChIP-qPCR, Sub-telomere Forward	ATTCATGAAGGGGTGGAGCC	N/A
ChIP-qPCR, Sub-telomere Reverse	TGCACCTCAGCCGGAC	N/A
ChIP-qPCR, LTR10C Forward	CAAGTCAGTTGTCCTAGCTTGC	N/A
ChIP-qPCR, LTR10C Reverse	GGAATGGCATGCACTATGGG	N/A
CRISPR/Cas9, Control Olig Forward	CACCGTGCTCCGTGCATCTGGCATC	N/A
CRISPR/Cas9, Control Olig Reverse	AAACGATGCCAGATGCACGGAGCAC	N/A
CRISPR/Cas9, SubTelo4-0.5k Olig1 Forward	CACCGGGGTTAGGGTTAGGGTTTTA	N/A
CRISPR/Cas9, SubTelo4-0.5k Olig1 Reverse	AAACTAAAACCCTAACCCTAACCCC	N/A
Recombinant DNA		
siRNA-*ZSCAN4*	Ribo Bio	Cat #siG12424100122-1-5 #siG12424100134-1-5 #siG12424100143-1-5
siRNA-NC	Ribo Bio	Cat #siNoooooo1-1-10 siN0000002-1-10
Software and algorithms		
TFL-Telo	http://www.bccrc.ca/tfl/people_plansdor.html	N/A
Graphpad Prism8	https://www.graphpad.com/scientific-software/prism/	N/A
Adobe Illustrator	https://www.adobe.com/products/illustrator.html	N/A

(*Continued on next page*)

Continued

REAGENT or RESOURCE	SOURCE	IDENTIFIER
ZEN 2.3(blue edition)	https://blogs.zeiss.com/microscopy/en/zen-imaging-software-for-microscopy-new-quick-guides-tutorials-available/	N/A
Other		
LightCycler 480 II System	Roche	N/A
FV1000 laser confocal fluorescence microscope	Olympus	N/A
HiFi Hot-Start ReadyMix	KAPA Biosystems	N/A
Celldiscoverer7 LSM900	ZEISS	N/A

RESOURCE AVAILABILITY

Lead contact

Further information and reasonable requests for resources and reagents should be directed to and will be fulfilled by the lead contact, Sicong Zeng (zengsicong@hunnu.edu.cn).

Materials availability

This study did not generate new unique reagents.

Data and code availability

- All data is available in the main text or the supplemental information. Original images and microscopy data will be shared by the lead contact upon request. This paper analyzes existing, publicly available data. These accession numbers for the datasets are listed in the key resources table.
- This paper does not report original code.
- Any additional information required to reanalyze the data reported in this paper is available from the lead contact upon request.

EXPERIMENTAL MODEL AND SUBJECT DETAILS

Patients

This study was approved and guided by the Ethics Committee of the Reproductive & Genetic Hospital of CITIC-Xiangya (LL-SC-2020-007). All sperm and immature oocytes were collected after obtaining written informed consent from the donor couples. The informed consent confirmed that the donor couples voluntarily donated sperm and immature oocytes for this research and received no financial compensation.

Collection of human material

Oocytes lacking both a polar body and germinal vesicle were collected. Immature oocytes were cultured at 37.5°C in an atmosphere of 6% CO_2, 5% O_2, and 89% N_2; and the medium used was commercial IVM medium (Vitrolife, Göteborg, Sweden) supplemented with 0.075 IU/mL FSH, 0.5 IU/mL hCG, 1 μg/mL estradiol, and 0.5% human serum albumin (HSA). Only those oocytes that expelled the first polar body within 4–8 hours after *in vitro* culture were collected and prepared for further experiments. Human embryos were obtained from *in vitro* matured oocytes by conventional ICSI, and fertilized embryos were transferred to the wells of a pre-equilibrated EmbryoSlide (Vitrolife, Cat#16350) and cultured in G-1 Plus medium (Vitrolife, Cat#10127). Slides containing embryos were immediately placed in an Embryoscope chamber and cultured at 37.5°C in 6% CO_2, 5% O_2, and 89% N_2; with the culture medium changed on day 3. All human embryos used in this study exhibited normal morphology with an appropriate developmental rate.[29]

Animals and collection of mouse embryos

To obtain spermatozoa, oocytes, and preimplantation embryos, we first housed C57BL/6 male and female mouse (6–8 weeks of age) in the animal facility of the Reproductive & Genetic Hospital of CITIC-Xiangya. The cauda epididymis was removed from one male, cut, and the semen squeezed out. Sperm were placed

in 1.5-mL EP tubes with 500 μL of G-IVF medium and incubated at 37°C for 20 min to allow them to swim out. The female mouse was each superovulated by injection with 10 IU of pregnant mare serum gonadotropin (PMSG), followed by an injection of 10 IU of human chorionic gonadotropin (HCG) 48 h later. The superovulated female mouse was mated with C57BL/6 male mouse, and zygotes, early-two-cell, mid-two-cell, and late-two-cell stage embryos were flushed from the oviducts of the female mouse at 24 h, 31 h, 40 h, and 48 h after HCG injection, respectively. Four-cell, eight-cell, and 16-cell stage embryos were flushed from the uteri of the female mouse at 55 h, 70 h, and 78 h after injection, respectively; and MII oocytes were collected from the oviducts of unmated female mouse.

Cell culture

The human ES cell lines chHES-8, chHES-8 *p53*$^{-/-}$, chHES-90, and chHES-137 that we adopted herein were established at the National Engineering Research Center of Human Stem Cells. The cell lines were routinely tested for mycoplasma contamination and were negative throughout the current study. The hESCs were plated on MEF feeders and cultured in Dulbecco's modified Eagle's medium/F-12 supplemented with 15% knockout serum replacement, 2 mM nonessential amino acids, 2 mM l-glutamine, 0.1 mM β-mercaptoethanol, and 4 ng/mL human recombinant basic fibroblast growth factor (bFGF) (all ingredients were from Invitrogen, Oslo, Norway). The medium was changed daily until embryonic outgrowth was observed, and we then transmitted the outgrowth onto fresh MEF feeder layers and assessed hESC-colony morphology during prolonged culture. hESCs colonies were mechanically passaged every seven days. hESCs were mechanically isolated and then plated on Matrigel (354234, Corning)-coated plates in mTeSR1 (05850, STEMCELL) with 10 μM ROCK inhibitor Y-27632 (688002, Calbiochem) for subsequent treatments. After 24 h, the medium was changed with mTeSR, and replaced every day thereafter. For BIX01294 treatment, 2.7 μM BIX01294 (Selleck, China) was added to feeder-free cultured hESCs in mTeSR medium.

METHOD DETAILS

Immunofluorescence microscopy

Zonae pellucidae were removed by a brief incubation with acidic Tyrode's solution, and zona pellucida-free embryos were washed in phosphate-buffered saline (PBS), fixed in freshly prepared 2% paraformaldehyde for 20 min at room temperature, and washed twice in PBS. Afterward, the embryos were permeabilized in 0.5% Triton X-100 for 25 min, washed three times in PBS, and then blocked with 5% donkey serum for 1 h. Samples were incubated with SIN3A antibody (Cat #3479, Abcam), TRF2 antibody (Cat #ab108997, Abcam), or rabbit polyclonal anti-γH2AX antibody (Cat #80312, Cell Signaling Technology) diluted 1: 100 in blocking solution at 4°C overnight, washed three times, incubated with FITC donkey anti-mouse IgG or FITC anti-rabbit IgG for 1 h at room temperature in the dark, washed again, and finally mounted with VECTASHIELD mounting medium and exposed to 0.5 μg/mL 4, 6-diamidino-2-phenylindole (DAPI, 1 μg/mL, Thermo Fisher Scientific). Images were captured with a ZEISS microscope equipped with fluorescence (Celldiscoverer 7 with LSM900).

Telomere Q-FISH

Oocytes and embryos were treated with a hypotonic solution (1% sodium citrate) followed by fixation in methanol: acetic acid (3: 1), and then spread on a glass slide. After washing with PBS, the slides were treated with pepsin (0.1%) at 37°C for 10 min; dehydrated through a gradient of 70, 90, and 100% ethanol; and air-dried. Telomeres were denatured at 80°C for 3 min and hybridized for 2 h with FITC-labelled (CCCTAA)3 peptide nucleic acid (PNA Bio, Korea) probe at 0.5 μg/mL. The slides were then washed with 70% formamide solution twice and PBS three times before dehydration through the graded ethanol series and air-drying. Chromosomes were stained with 0.5 μg/mL DAPI, and chromosomes and telomeres were digitally imaged on a Leica microscope using FISH 2.0 software. For quantitative measurements of the telomere length, telomere fluorescence intensity was integrated using the TEL-TELO program (freely available from the Flintbox Network at www.flflintbox.com). We estimated the telomere length based on the relative fluorescence intensity using standard cell lines (L-5178Y-S) of known telomere lengths, which were then added to the slides when the samples were fixed. Sperm samples were required to achieve sperm head decondensation before Q-FISH. Briefly, sperm were washed with PBS twice and spread on a glass slide followed by fixation in methanol: acetic acid (3: 1), and slides were treated with 0.8 M DTT for 7 min and air-dried. After washing, the slides were dehydrated through a graded ethanol series and placed in the oven overnight, with hybridization subsequently performed as described above. Q-FISH is a modality used for precise quantification based upon fluorescence intensity, such that the exposure intensity exerts a

large influence on the results during the experimental operation. In order to avoid drift in the linear relationship between telomere fluorescence intensity and telomere length due to too strong or too weak an exposure, and exclude the detection error caused by the fusion of telomeres at chromosome ends, we optimized the telomere signal according to the data published previously to exclude the interference caused by overlapping signals or background signals, and chose a standard cell line with known telomere length as the control and plotted the linear curve of fluorescence intensity vs. telomere length according to L-5178Y-S—the known telomere length at standard exposure time for the detection of embryonic telomeres. To ensure a parallel and consistent fluorescence signal, all image acquisitions were conducted at the end of hybridization. Since not all embryos provided a complete karyotype, we excluded signal points with strong signals outside of the end-fused chromosomes and nuclei.

Telomere measurement by quantitative PCR

Average TL was analyzed by real-time quantitative PCR as described previously. Briefly, genomic DNA was extracted from hESCs using the QiaAmp DNA Kit (Qiagen). The Ct value for the telomere (T) and the Ct value for the single-copy gene (S) were recorded in separate PCR runs. We implemented standard curves for the assay by employing standard hESCs samples of known telomere lengths in our laboratory.[44] LightCycle 480 software (Roche) was used to generate the standard curves and Ct values. The T/S ratio represents the relative telomere length compared to standard hESCs.

Single-oocyte and embryonic quantitative reverse-transcription PCR (RT-qPCR)

After oocytes and embryos were collected at the different stages, cDNA libraries were generated using the Smart-seq2 protocol as described previously.[28] Briefly, the zonae pellucidae were removed using acidic Tyrode's solution (Sigma, St. Louis, MO, USA) and the samples were placed in PCR tubes. Following cell lysis, mRNA was released and the oligo-dT primer was added at 72°C for 3 min. For first-strand cDNA synthesis, the RT reaction was executed using SuperScript II reverse transcriptase (Invitrogen, Gaithersburg, MD, USA). The cDNA was then amplified by PCR (18 cycles) using a KAPA HiFi Hot-Start ReadyMix (KAPA Biosystems, Boston, USA) and purified using Ampure XP beads (Beckman Coulter, Brea, CA, USA). The cDNA of single oocytes or embryonic equivalents was used as a template for real-time PCR analysis in a Roche LightCycler 480 II System (Roche, Basal, Switzerland) using a FastStart Universal SYBR Green Master mix (Roche). Samples were amplified in triplicate to ensure amplification integrity. The PCR conditions were as follows: 95°C for 5 min; followed by 45 cycles of 95°C for 15 s, 58°C for 10 s, and 72°C for 10 s. The relative expression levels of each target gene compared to β-actin were calculated using the comparative threshold cycle ($2^{-\Delta\Delta CT}$) method. Specific PCR primer pairs are depicted in key resources table.

Total RNA isolation, reverse transcription, and quantitative PCR

Total RNA was prepared using TRIzol reagent (Invitrogen, Oslo, Norway), and cDNA was obtained by reverse transcription using a Transcriptor First Strand cDNA Synthesis Kit (Roche, Switzerland) according to the manufacturer's instructions. Quantitative PCR was performed on a LightCycler 480 II PCR system (Roche, Switzerland) using an SYBR Green PCR mix (Roche, Switzerland). Relative expression was quantified using the comparative cycle threshold method, and threshold cycles were normalized to GAPDH. DNA pulled down by ChIP assays was amplified by quantitative PCR.

Western blot analysis

Cellular protein from the treated group was extracted with the Nuclear and Cytoplasmic Extraction Kit (CWBIO, China), and equal amounts of protein were resolved using 10% SDS-PAGE and electro-transferred to polyvinylidene difluoride (PVDF) membranes. The membranes were blocked with TBST containing 1% BSA for 1 h at room temperature, and then incubated overnight with p53 Antibody (DO-1) at 4°C and goat anti-mouse IgG-HRP (Santa Cruz) in 1% BSA in TBST at room temperature for 1 h. After washing with TBST, the membranes were analyzed with ECL chemiluminescence (Thermo Fisher Scientific, USA).

CRISPR/Cas9

CRISPR sgRNAs targeting the sites of human subtelomere regions at 0.5 kb and 1.0 kb from the telomeric end were designed as previously described,[57] and we designed primers for the appropriate restriction sites. The double-stranded primers were annealed to a single strand and cloned into a modified Lenti-CRISPR containing a puromycin cassette and BsmB I endonuclease. Two packaging plasmids (N75 and VSV-G) and vectors containing sgRNA (Lenti-CRISPR-puromycin) were co-transfected into the convergence

of 80% of the 293 T cells using the transfection reagent Lipofectamine 2000 (Invitrogen, Oslo, Norway). The sgRNA-containing virus-particle supernatant was then collected and passed through a 0.45-μm filter. For viral infection, 2×10^6 ES cells were exposed to lentiviral supernatant for 24 h in the presence of polybrene (Sigma, MO, USA), and after 48 h the cells were selected using 3 μg/mL puromycin for 4 days. The remaining cells were passaged on MEFs for single-colony selection, and puromycin-resistant clones were chosen and then analyzed by sequencing. Genomic DNA was extracted using the QIAamp DNA Mini kit (Qiagen, China), with the following primers used for the PCR amplification reaction: forward, 5′-CCCATCTA CATCCCCCTTG-3′ and reverse: 5′-CAGGAAGCCAAAGGGTGAAGA-3′. The PCR products were submitted to a biological company (Qingke Biological Company) for TA cloning, and the recovered fragments were randomly connected to the T carrier. The T-vector containing the target fragment was transformed into DH-5α cells and evenly spread on LB solid medium.

Chromatin immunoprecipitation assay

Chromatin immunoprecipitation (ChIP) assays were performed using the EZ-ChIP Kit from Millipore according to the manufacturer's protocol. Samples were assessed by applying anti-H3K9me3 (Cat #13969, Cell Signaling Technology), and anti-p53 (A0263, Abclonal) antibodies.

Microinjection of small interfering RNAs (siRNAs) and embryo culture

The siRNA generated against mouse *Zscan4* was diluted in nuclease-free water to 20 μM, and zygotes were injected with approximately 10 pL of siRNA using an injection needle (Femtotips II™, Eppendorf, Hamburg, Germany). The injected embryos were observed and their derived data summarized from the early-two-cell stage to the four-cell stage. CZB medium was employed for embryo culture in an atmosphere of 5% CO_2 in compressed air. For embryo incubation, CZB was overlaid with sterile mineral oil (Sigma, MO, USA). The siRNAs sequences were designed and synthesized by RiboBio (Guangzhou, China).

QUANTIFICATION AND STATISTICAL ANALYSIS

All assays were repeated three times and all samples were analyzed in triplicate. The data are expressed as the mean ± SD of at least three independent experiments. *t* test was used to determine the significance of differences between and among groups, respectively; and $p < 0.05$ was deemed statistically significant. Curve-fitting analyses were conducted using GraphPad Prism Software 8.0 (GraphPad Software, USA).